HHS Public Access

Author manuscript

Nat Biomed Eng. Author manuscript; available in PMC 2017 October 10.

Published in final edited form as:

Nat Biomed Eng. 2017 ; 1: . doi:10.1038/s41551-017-0058.

Rapid magnetic isolation of extracellular vesicles via lipid-based nanoprobes

Yuan Wan[1,2], **Gong Cheng**[1,2], **Xin Liu**[3,4], **Si-Jie Hao**[1,2], **Merisa Nisic**[1,5], **Chuan-Dong Zhu**[1,6], **Yi-Qiu Xia**[1,2], **Wen-Qing Li**[1,2], **Zhi-Gang Wang**[1,2], **Wen-Long Zhang**[1,2], **Shawn J. Rice**[3,4], **Aswathy Sebastian**[7], **Istvan Albert**[5,7], **Chandra P. Belani**[3,4], and **Si-Yang Zheng**[1,2,5,8]

[1]Department of Biomedical Engineering, Micro & Nano Integrated Biosystem (MINIBio) Laboratory, The Pennsylvania State University, University Park, PA 16802, U.S.A

[2]Penn State Materials Research Institute, The Pennsylvania State University, University Park, PA 16802, U.S.A

[3]Penn State Milton S. Hershey Medical Center, The Pennsylvania State University, Hershey, PA 17033, U.S.A

[4]Penn State Hershey Cancer Institute, The Pennsylvania State University, 500 University Drive, Hershey, PA 17033, U.S.A

[5]The Huck Institutes of the Life Sciences, The Pennsylvania State University, University Park, PA 16802, U.S.A

[6]The Second Hospital of Nanjing, Affiliated to Medical School of Southeast University, Nanjing, China, 210003

[7]Department of Biochemistry and Molecular Biology, The Pennsylvania State University, University Park, PA 16802, U.S.A

[8]Department of Electrical Engineering, The Pennsylvania State University, University Park, PA 16802, U.S.A

Abstract

Extracellular vesicles (EVs) can mediate intercellular communication by transferring cargo proteins and nucleic acids between cells. The pathophysiological roles and clinical value of EVs are under intense investigation, yet most studies are limited by technical challenges in the isolation of nanoscale EVs (nEVs). Here, we report a lipid nanoprobe that enables spontaneous labelling

Corresponding author: Si-Yang Zheng, sxz10@psu.edu.

Author contributions

Y.W. and S.-Y.Z. designed the research. Y.W. conducted experiments and analysed data. G.C. prepared the magnetic sub-micrometre particles, assisted with peptide-sample preparation and performed proteomic analyses. S.-J. H. assisted in the preparation of NGS samples, in RNA NGS data analysis, and in fluorescence imaging. M.N. prepared blood plasma. C.-D.Z. and W.-Q.L. assisted in cell culture, nEV collection and gel electrophoresis. Y.-Q.X. performed the wound-healing assay. Z.-G.W. performed the electron microscopy. W.-L.Z. assisted in image processing. A.S and I.A analysed NGS DNA data. X.L., S.J.R. and C.P.B. recruited patients and provided blood samples, tissue NGS data, and clinical support. Y.W. and S.-Y.Z. wrote the manuscript.

Competing interests

The authors declare no competing financial interests.

and magnetic enrichment of nEVs in 15 minutes, with isolation efficiency and cargo composition similar to what can be achieved by the much slower and bulkier method of ultracentrifugation. We also show that the lipid nanoprobes, which allow for downstream analyses of nucleic acids and proteins, enabled the identification of *EGFR* and *KRAS* mutations following nEV isolation from blood plasma from non-small-cell lung-cancer patients. The efficiency and versatility of the lipid nanoprobe opens up opportunities in point-of-care cancer diagnostics.

Extracellular vesicles — which include exosomes, microvesicles and apoptotic bodies — are cell-derived lipid-bilayer-enclosed structures, with sizes ranging from 30 nm to 5,000 nm (ref. [1]). In the past decade, EVs have emerged as important mediators of cell communication because they serve as vehicles for the intercellular transmission of biological signals capable of altering cell function and physiology[2,3]. In particular, exosomes — that is, EVs with diameters in the 30–150-nm range, released upon the fusion of multivesicular bodies with the plasma membrane[1,3,4] — containing cell and cell-state specific proteins and nucleic acids are secreted by many cell types and have been identified in diverse body fluids. Although the biogenesis of exosomes is still not yet fully understood[5–10], growing evidence indicates that such nEVs can regulate tumour immune responses, initiate the formation of the pre-metastatic niche, determine organotropic metastasis, and contribute to chemotherapeutic resistance[11,12]. nEVs are thus potential targets for therapeutic intervention in cancer, and are promising as autologous drug vehicles capable of overcoming pharmacological barriers[13,14]. They are also increasingly recognized as non-invasive diagnostic and prognostic tumour markers[15,16]. Hence, it is highly desirable to isolate nEVs rapidly for downstream molecular analyses. However, approaches reported for the isolation of nEVs — such as ultracentrifugation, immunoisolation, polymer-based precipitation, and filtration — involve lengthy protocols, and can lead to isolation biases, to the presence of impurities, and to nEV damage[17].

Here, we report a lipid nanoprobe (LNP) for the rapid isolation of nEVs, including exosomes from serum-free cell-culture supernatant and from blood plasma. The approach involves the labelling of the lipid bilayer of nEVs with a biotin-tagged 1,2-distearoyl-sn-glycero-3-phosphethanolamine-poly(ethylene glycol) (DSPE-PEG) probe. The labelled nEVs can then be collected by NeutrAvidin (NA)-coated magnetic sub-micrometre particles (MMPs), for subsequent extraction and analyses of nEV cargo (Fig. 1). Compared with differential centrifugation (the prevalent method for nEV isolation), the LNP shortens the isolation procedure from over 22 h to 15 min and doesn’t require bulky or expensive equipment. It is also highly flexible and can be adopted for various downstream analyses of DNA, RNA and proteins. We applied the LNP to obtain nEV DNA from 19 stage-IV non-small-cell lung-cancer (NSCLC) patients, which allowed us to detect mutations in KRAS (V-Ki-ras2 Kirsten rat sarcoma viral oncogene homologue) codons 12 and 13 and EGFR (epidermal-growth-factor receptor) exons 19 and 21.

Results

Design, optimization, and characterization of the LNP

The LNP consists of a labelling probe (LP) and a capture probe (CP). The LP is composed of a lipid tail for nEV membrane insertion, a PEG spacer (about 45 ethylene oxide units, giving approximately 156 Å of spacer length) for increasing reagent solubility, and a biotin tag for subsequent isolation of labelled nEVs (Fig. 1, middle). We first compared the labelling efficiency among fluorescein isothiocyanate (FITC)-conjugated PEGylated monoacyl lipid (C18), diacyl lipid (DSPE) and cholesterol. Because both cell membranes and EV membranes are lipid bilayers, to facilitate evaluation we used 10^7 breast adenocarcinoma MDA-MB-231 cells in Diluent C or 5% human albumin in phosphate-buffered saline (Supplementary Fig. 1a). Although the presence of human albumin significantly decreased the fluorescence intensity of cells labelled with PEGylated lipids in comparison with the fluorescence intensity for the Diluent-C group ($p < 0.05$; two-tailed t-test), in the presence of albumin the three lipids show differential labelling efficiencies (Supplementary Fig. 1b). The average fluorescence intensity of C18-labeled cells in 5% human albumin is slightly higher than that of cells labelled with DSPE, but there is no significant difference between the two groups. Considering that diacyl lipids have been widely used for the manipulation of cells and that the mechanism is known, we chose DSPE-PEG-biotin as the LP for the following studies.

The NA-coated MMPs serve as the CP and enable the enrichment and isolation of nEVs in suspension. The MMPs were prepared as a monodisperse suspension with a mean size of 465.4 nm (Fig. 2a). Raw MMPs present a negative zeta potential of –32.0 mV (Supplementary Fig. 2a), arising from their silica shell. After aminosilane modification, absorption peaks at 2,920 cm^{-1} and 2,852 cm^{-1} in the spectra of Fourier transform infrared spectroscopy (Supplementary Fig. 2b), associated with the stretching vibration of methylene groups of silane, indicate the immobilization of amine groups. Accordingly, the value of the zeta potential shifts to 9.6 mV and then decreases to –17.7 mV once isothiocyanate is conjugated. The surface-modification process was finalized with the covalent immobilization of NA (Methods).

Nanoscale extracellular vesicles from MDA-MB-231 cells were isolated with ultracentrifugation, and identified by electron microscopy (EM). The isolated nEV population mainly consisted of vesicles within the diameter range of 30–200 nm (Supplementary Fig. 3a) exhibiting the characteristic saucer-shaped morphology under the EM (Fig. 2b, Supplementary Fig. 3b) and the usual spherical shape under the cryo-scanning electron microscope (Fig. 2c). nEVs captured on MMPs were imaged with cryo-scanning electron microscopy (cryo-SEM) and transmission electron microscopy (TEM) (Fig. 2d, Supplementary Fig. 3c). We also show that nEVs labelled with DSPE-PEG-FITC can be effectively uptaken and internalized by MDA-MB-231 cells (Supplementary Fig. 4). nEV pellets were homogeneously re-suspended in serum-free medium and divided in sextuplicate for the preparation of model samples. Each model sample contained approximately 1.4×10^9 nEVs, as measured by NanoSight (Supplementary Fig. 5a) and on average 348.5 ng of total RNA and 189.4 ng of DNA, as determined by Agilent Bioanalyzer and TapeStation,

respectively (Supplementary Figs 5b and 5c). We first evaluated the effect of the amount of LP, ranging from 1 pmol to 10 nmol, on nEV isolation efficiency (mass fraction of RNA extracted from the captured nEVs over total nEVs). Isolation efficiency increased gradually with increasing amounts of LP, with the maximum efficiency of 77.6% corresponding to 10 nmol of LP. An additional amount of LP did not further increase the isolation efficiency (Fig. 2e). Next, we determined the effect of incubation time on the isolation of nEVs with 10 nmol of LP. Although there was a gently increase in average isolation efficiency with incubation time (Fig. 2f), prolonged incubation didn't bring any statistically significant benefit ($p > 0.05$; two-tailed t-test). For operability and reliability reasons, we incubated LP with nEVs for 5 min (the duration regularly employed for exosome *in vitro* staining via membrane dye PKH26; ref. [18]). Also, we found that the incubation period for maximum isolation efficiency can be shortened to 10 min with continuous gentle rotation (Fig. 2g). Altogether, approximately 80% of nEVs from the model sample can be labelled and isolated using 10 nmol of LP and CP in excess, with the whole isolation procedure taking about 15 min.

In addition, when we used DSPE-PEG-Desthiobiotin as LP, captured MDA-MB-231 nEVs on MMPs can be released through displacement of DSPE-PEG-Desthiobiotin with biotin, which binds much more tightly to NA than desthiobiotin. Approximately 84 ± 3% of the nEVs were released within 30 min (cryo-TEM images of MDA-MB-231 nEVs harvested by ultracentrifugation and of the LP-labelled nEVs are shown in Supplementary Figs 6a and 6b). Furthermore, the released nEVs are functional. We educated non-invasive MCF7 cells with ~8×10^8 nEVs derived from highly aggressive MDA-MB-231 cells. A wound-healing assay showed the wound-closure rate of MCF-7 cells to be about two-fold faster upon nEV education ($p < 0.05$; two-tailed t-test), which indicates that the LP-labelled nEVs can induce higher levels of migration than uneducated MCF-7 cells (Supplementary Figs 6c and 6d). We then applied the LNP to isolate nEVs from blood plasma. Because albumin might interfere with the insertion of LP into the membrane of nEVs, we increased its amount up to 200 nmol in order to label and isolate nEVs from 100 μl of blood plasma from a healthy donor containing approximately 13.2 ng RNA, as determined by a Qubit fluorometer. An isolation efficiency of 48.3% was reached with 100 nmol of LP and CP in excess. Doubling the LP amount only slightly increased the efficiency to 49.5% (not statistically significant; $p > 0.05$, two-tailed t-test; Fig. 2h).

Detection of nucleic acids and proteins in model nEV samples

The LNP enables nEV enrichment directly onto a surface, which facilitates subsequent molecular analyses for the quantitative detection of nEVs and the profiling of membrane proteins. After incubation of the LP with model MDA-MB-231 nEV samples for 5 min, the mixture was transferred into NA-coated wells on a multi-well plate for nEV capture. Here, NA was immobilized on the well surface, and the NA–biotin reaction time was extended to 30 min, which allowed for over 95% binding efficiency[19]. We used a membrane-permeant dye (SYTO RNASelect) to selectively stain nEV RNA, and found that the green fluorescence intensity increased in direct proportion to total RNA contained in integral nEVs ($r^2 = 0.98147$; Fig. 3a). This demonstrates that this assay can semi-quantify nEV RNA

content in 35 min, which could be a useful alternative when nanoparticle-tracking or dynamic-light-scattering equipment is not available.

Proteins in the nEV membrane can also be detected by using LNP-mediated capture and enrichment. Model nEVs from neuroblastoma SK-N-BE(2) cells, breast adenocarcinoma MDA-MB-231 cells, and colon adenocarcinoma SW620 cells were captured and stained with fluorescently labelled anti-CD9 or anti-EpCAM antibodies (Fig. 3b). CD9 is one of the most ubiquitous molecular markers for all EVs(ref. [20]), and anti-EpCAM DynaBeads (life technologies) have been widely used for exosome isolation[21]. EpCAM expression in nEVs from SK-N-BE(2) cells was barely detected, whereas the expression levels for nEVs from MDA-MB-231 and SW620 cells were weak and strong, respectively. On the other hand, the expression levels of CD9 were comparable among nEVs from these three cell lines. These results parallel those of the expression of EpCAM and CD9 determined by immunocytochemistry (Fig. 3b, top).

Nanoscale extracellular vesicles can also be directly collected by CPs, followed by the extraction and analysis of protein and nucleic-acid cargo. CD63 (a commonly used EVs marker[22]) and GAPDH (a well-known housekeeping protein) extracted from MDA-MB-231 cell lysates and nEV protein lysates, respectively, were detected by western blot (Fig. 3c, Supplementary Fig. 7). Additionally, DNA and RNA were extracted from isolated MDA-MB-231 nEVs followed by agarose gel electrophoresis to confirm the presence of RNA and long fragments of DNA (Fig. 3d, Supplementary Fig. 8)[9,10,23].

We also compared the contents of nEVs harvested by ultracentrifugation and by the LNP. DNA from MDA-MB-231 nEVs and cellular genomic DNA without amplification were analysed by next-generation sequencing (NGS). The purified nEV DNA samples mainly contained DNA fragments longer than 10 kbp (Supplementary Fig. 5c). This differs from circulating cell-free DNA, which shows a typical apoptotic DNA ladder[24]. The percent of reads mapped to the human genome was 99.6% and 99.5% in the ultracentrifugation and LNP groups, respectively. DNA from nEVs isolated by the two methods uniformly spanned all chromosomes. The nEV DNA contents after ultracentrifugation and LNP isolation were similar, with a Pearson correlation coefficient (PCC) of 0.96 calculated using a 100-kbp window size (Fig. 3e). The nEV DNA content extracted by either of the two methods resembles nuclear genomic DNA from the same cell line, as indicated by the copy-number-variation (CNV) plots of the purified nEV samples and of the genomic DNA sample (Supplementary Fig. 9). In addition, the PCCs between the nEV DNA content of ultracentrifugation and the genomic DNA content and between the nEV DNA content of LNP and the genomic DNA content were 0.87 and 0.92, respectively.

Moreover, cargo RNA was extracted from nEVs isolated by ultracentrifugation and the LNP, and then compared. Quadruplicated MDA-MB-231 nEV RNA, including mRNA and miRNA, were analysed by NGS. The average percent of reads mapped to human total RNA was 89.3% and 86.2% for the ultracentrifugation and LNP groups, respectively. In an Euclidean-distance plot of mRNA from MDA-MB-231 nEVs (Supplementary Fig. 10a), the biological replicates isolated with the LNP and those isolated by ultracentrifugation appeared in separate clustered regions. Using read counts of mapped sequences, we then

quantified the RNA cargo of nEVs isolated from MDA-MB-231 cells with the LNP and with ultracentrifugation. nEVs isolated from MDA-MB-231 cells contained diverse cargo RNA, including significant amounts of lincRNA, rRNA, snoRNA, and other RNA types in addition to the most abundant RNA type, protein-coding RNA or mRNA (Fig. 3f). There were no noticeable differences in RNA species between nEVs isolated by the LNP and by ultracentrifugation; in fact, there was a substantial overlap of mRNA (81%) and miRNA (94%) species in the top-1000 expressed mRNAs and miRNAs (Supplementary Fig. 10b, Supplementary datasets 1 and 2). In a Bland–Altman plot (Supplementary Fig. 10c) comparing the expression levels of mRNAs isolated by ultracentrifugation or the LNP, we found that the majority of the detected mRNAs had similar expression levels, also indicated by the linear correlations with correlation coefficients > 0.998 for total RNA content (Supplementary Fig. 8d). A recent report indicated that fetal bovine serum (FBS)-derived miRNAs interfere with subsequent transcription analysis[25]. We however found minimal interference by the reported top 14 FBS miRNAs when comparing the numbers of miRNAs in the nEV samples collected by ultracentrifugation and by the LNP (Supplementary Table S1).

Furthermore, we found that after nEV isolation by the LNP the weight ratio of protein to RNA in extracts decreased from 12.1 to 4.9 (Supplementary Fig. 11a), indicating that without an additional washing step our approach can eliminate on average 68.5% of total protein. Because nEV isolation by the LNP leads to a 22% loss of nEVs, we speculate that the removed protein consists mainly of protein contaminants. Instead, ultracentrifugation harvests 61.4% of nEVs from a model sample. Additional wash purification by re-suspension in PBS and extra ultracentrifugation reduces the efficiency to only 13.9% (Supplementary Fig. 11b). Results from liquid chromatography-tandem mass spectrometry (LC-MS/MS) further revealed the relationship between cargo proteins of nEVs collected by ultracentrifugation and by the LNP (Supplementary dataset 3). We compared our LC-MS/MS data with a recently published report[26] on 30 key proteins in EVs (Supplementary Table S2). We found a similar composition of cargo proteins in nEVs isolated by ultracentrifugation and by the LNP. Moreover, our results are also consistent with the work in ref. [26], which used a combination of ultracentrifugation and density-gradient ultracentrifugation for small EV preparation. In addition, for 8,452 EV cargo proteins archived in the public database Vesiclepedia (www.vesiclepedia.org), we found that ~91% and ~94% of them corresponded to the cargo proteins from nEVs isolated by ultracentrifugation and by the LNP, respectively. Similarly, ~94% of the EV cargo proteins reported in ref. [26] can be identified in the database (Supplementary Fig. 12a). Also, 76, 89, and 96 out of the top 100 proteins from Vesiclepedia were identified in the nEVs isolated by ultracentrifugation, by the LNP, and in ref. [26], respectively (Supplementary Fig. 12b). And analysis of the cellular distribution of the identified proteins showed that, for the ultracentrifugation, LNP and ref. [26] groups, respectively, 51.8%, 64.7%, and 57.2% of these proteins localize with exosomes and 34.2%, 39.7%, and 47.6% localize with lysosomes ($p < 0.01$; two-tailed t-test; Supplementary Fig. 12c). Additionally, our MS analysis also confirmed that vimentin, cytokeratin, EGFR, and the mammary cancer stem cell marker CD44 appear in the nEVs from MDA-MB-231 cells, which agrees with the phenotype of this triple-negative and aggressively metastatic cancer cell line.

Detection of mutated DNA in nEVs isolated from blood-plasma samples from NSCLC patients

By using the LNP, we isolated nEVs from 100-μl blood-plasma samples of 19 NSCLC patients. To achieve high sensitivity, we implemented mutant-enriched PCR assays for the analysis of mutations in EGFR exons 19 and 21, and a real time PCR assay for the identification of mutations in KRAS codons 12 and 13 (Supplementary Fig. 13)[27]. All PCR products were subjected to Sanger sequence analysis. After conventional PCR amplification, desired PCR products of EGFR exon 19 and 21 and of KRAS were obtained from all samples (Fig. 4a and Supplementary Fig. 14). Sequencing analysis only identified the KRAS G13D mutation in the plasma sample of patient 42 (Fig. 4b), and the finding was further confirmed by NGS of the patient's tumour tissue. Mutations were not detectable in the rest of the samples by Sanger sequencing of traditional PCR products (Supplementary Fig. 15). As the limit of detection (LOD) of mutant alleles for Sanger sequencing is about 10%, we employed a mutant-enriched PCR assay that can significantly push the LOD down to approximately 0.05% [27]. After mutation-specific restriction enzyme digestion and nested PCR, we found an L858R mutation in EGFR exon 21 in the plasma sample of patient 28 (Fig. 4c), which we were unable to confirm by NGS using the patient's tissue sample because of the low amount of sample available. Moreover, a deletion mutation in the EGFR exon 19 was readily detected in patient 29, which matched with the results of NGS sequencing of this patient's tissue sample (Fig. 4d). We also used real-time PCR to enrich mutations in KRAS codons 12 and 13 for downstream sequencing (Fig. 4e; according to the manufacturer, the LOD can reach 0.01% by targeting the mutant gene and suppressing the wild-type copy), which confirmed the KRAS G13D point mutation in the plasma sample of patient 42 (Fig. 4f). And a KRAS G12D mutation was detected in the plasma of patient 51, which was later verified by NGS of the patient's tissue sample (Fig. 4g). However, we failed to detect KRAS mutations in patient 25, 27 and 50 (Table 1), presumably because of their extremely low abundance in the nEVs in patient blood samples or of a change in mutation status in-between the times of primary tissue biopsy and blood draw. All wild-type EGFR and KRAS alleles in patient tissue samples were detected as wild-type after nEV isolation via the LNP.

Discussion

To increase the clinical utility of EVs, efficient isolation and detection methods are needed[28]. As phospholipid derivatives, PEGylated lipids have been used for the labelling and manipulation of cells and liposomes[29,30]. Similarly, PEGylated lipids can also be used for nEV isolation. The main advantage of the LNP approach described here is rapid nEV isolation. The two-step isolation procedure takes only 15 min; existing methods require however longer processing time, from 30 min to over 22 hours[17]. Also, the LNP system does not require bulky and expensive instruments or delicate microfluidic devices[31,32]. Moreover, the nEV isolation efficiency of the LNP system and of ultracentrifugation are similar. The EV isolation efficiency of ultracentrifugation depends on repeated cycles, however, and such additional purification step can damage the nEVs and reduce yields from ~70% to less than 10%[31]. By contrast, in the LNP system, repetitive purification is eliminated as ~68% proteins can be removed by the one-time isolation process, which exerts minimal impact on

downstream molecular analyses of the nEV content. Furthermore, the LNP system aids qualitative and quantitative molecular analyses of nucleic acid and proteins[33,34]. Altogether, by significantly shortening the time of sample preparation and by providing relatively pure nEVs via isolation, the LNP system should facilitate nEV-based diagnostics.

With regards to the lipids for membrane labelling, we found that DSPE bearing two hydrophobic fatty acid tails shows stronger non-covalent interactions with the lipid membranes of nEVs than sterol and monoacyl lipid with only one hydrophobic fatty acid tail, and thus that DSPE displays a relatively more stable retention[35]. It is worth noting that the optimal amount of LP and the isolation efficiency of nEVs vary for processing model samples and plasma. The difference could be ascribed to the presence, in plasma, of albumin and other lipoproteins that bind to LP (the binding constant of lipid and albumin is however only ~1×10^3 M^{-1} at room temperature[36]. Size differences between nEVs visualized by TEM and NanoSight (Supplementary Fig. 3a) might arise from either the shrinkage of nEVs during fixation, or from shortcomings in NanoSight that lead to a bias towards the detection of larger EVs.

Cells secrete heterogeneous populations of nEVs with different sizes and compositions[37,38], and universal EV markers such as CD63 do not consistently appear in each individual nEV (ref. [39]). Similarly, we found that the expression of EpCAM in nEVs harvested from three different cancer cell lines varied. This might however reflect low nEV-isolation efficiency with anti-EpCAM-based immunoisolation[40]. Conversely, the LNP system is unique in that it selects all lipid vesicles in the sample, thus providing antigen- and size-independent isolation performance. The method is therefore applicable to all nEVs regardless of size and protein composition. Overall, our genomic, transcriptomic, and small-RNA studies indicate that the cargo contents of the LNP-isolated nEVs are similar to those of nEVs isolated by ultracentrifugation. With low-coverage genomic sequencing, CNV profiles can be generated from purified nEV samples that are identical to the original cells. The DNA sequences obtained from LNP- and ultracentrifugation-isolated nEVs can not only be mapped to the human genome[9,10], but contain CNV profiles that are highly identical to the original MDA-MB-231 cells. This may provide a way to confirm the tumour of origin of nEVs. Read-counts-based quantitative analysis of the sequencing data reveals rich RNA content in nEVs isolated by LNP and by ultracentrifugation. Most of the reported cellular coding and noncoding RNAs are present in the isolated nEVs. In all cases, RNA from nEVs isolated by LNP exhibits insignificant differences with those from nEVs isolated by ultracentrifugation. Furthermore, protein LC-MS/MS analysis confirmed the similar protein compositions in nEVs isolated by the two methods, and our results are consistent with the Vesiclepedia database and a recent report on proteomic analysis of EV subtypes[26]. A cellular-distribution analysis further confirmed that LNP-isolated nEVs carry a large percentage of exosomal and lysosomal proteins.

nEVs contain whole genomic DNA[9], and mutated KRAS and p53 have been detected from exosomes pelleted from patient serum[10]. In such cohort study of patients with pancreatic cancer[10], mutation analysis on the basis of tumour tissue revealed that at least 1 and 4 patients carry mutations in EGFR exons 19 and 21 or in KRAS codons 12 and 13. This is in fair agreement with the frequency of EGFR (~5%) and KRAS (~15%) mutations in

NSCLC[41]. We harvested nEVs from NSCLC patients using the LNP system and extracted the genomic DNA for the detection of KARS and EGFR mutations. By using Sanger sequencing right after traditional PCR, we only identified the KRAS G13D mutation in one patient. Improving the detection sensitivity with mutant-enriched PCR and real-time PCR, we were able to find mutations in the DNA of nEVs from three more patient samples (we should note, however, that EGFR/KRAS mutations in the tissue samples and plasma samples might not be identical). A L858R mutation in the EGFR exon 21 and a G13D mutation in KRAS were identified in nEV DNA from two patients (28 and 42, respectively; there was however not enough sample available for tissue-based mutation analysis). This demonstrates the feasibility of mutation analysis in nEV DNA, and underscores the advantage of nEVs as a liquid-biopsy material, for which samples can be obtained easily and repetitively. KRAS mutations in three patients (25, 27 and 50) were undetectable in nEV DNA, probably because of extremely low allele fractions. Similar issues exist for mutation detection in circulating tumour DNA (ctDNA), so detection platforms and strategies developed for ctDNA might be adapted for nEV DNA. Digital PCR (dPCR), a sensitive tool that can detect mutations at 0.01% allele frequency, might resolve the discrepancy. dPCR enabled the identification of KRAS mutations in 48% of ctDNA from patients with primary pancreatic cancer[42]. By rearrangement of exons and introns covering recurrent mutations in potential driver genes, mutations in ctDNA could also be detected in 50% of patients with stage-I NSCLC[43]. This suggests that to for clinical diagnostics the analysis of nEV DNA would need a careful selection of cutting-edge technologies and detection strategies.

Methods

Collection of plasma samples

Normal control blood was obtained from consented donors at the Penn State General Clinical Research Center according to an institutional-review-board-approved protocol (IRB31216). Clinical samples were obtained with consent from advanced lung cancer patients at the Penn State Hershey Medical Center according to institutional-review-board-approved protocols (IRB 40267EP). Samples were drawn into 10-ml EDTA (K2) tubes (Vacutainer; Becton Dickinson) from peripheral venepuncture or from a central venous line. After centrifugation at 300*g* for 5 min and then at 16,500*g* for 20 min at 4 °C, plasma was collected, filtered using a 0.22 μm pore filter, and stored at –80 °C until processing.

Cell culture

MDA-MB-231, SW620 and SK-N-BE(2) cells were maintained in phenol-red-free-DMEM (Corning) supplemented with 10% (v/v) fetal bovine serum (FBS), 100 units/ml penicillin, 100 μg/ml streptomycin. Cells were cultured in a humidified atmosphere of 5% CO2 at 37 °C.

Preparation of model samples of nEVs

MDA-MB-231 cells were grown in 9 T75 flasks (Falcon) for 2–3 days until they reached a confluency of 80%. Next, cells were cultured in SFM (Corning) for 48 h. The medium was collected and centrifuged at 300*g* for 5 min followed by a centrifugation step at 16,500*g* for 20 min to discard cellular detritus. Afterwards, the medium was filtered using a 0.22-μm

pore filter. A total of 108 ml of medium was collected and ultracentrifuged at 100,000*g* without break at 4 °C for 2 h. The nEV pellets were suspended in 200 μl of SFM. A total of 400 μl of nEVs in SFM were divided into 6 equal parts. Standardization samples by triplicate were used to evaluate the efficiency of polymerizable lipids in the isolation of nEVs. The model samples were incubated with 10 μl of DNase I (1 U/μl, Life Technologies) or 5 μg/ml RNase at 37 °C for 2 h. The supernatant was collected and stored at –80 °C.

nEV cell uptake

nEVs in Diluent C were incubated with 2 μl PKH26 (Sigma-Aldrich) in Diluent C for 5 min at 4 °C before purification by ultracentrifugation. The uptake was performed by incubating cell cultures with labelled nEVs in 96-well plate for 2 hours at 37 °C. Cells were fixed with 4% paraformaldehyde at 4 °C for 10 min and stained with DAPI solution at concentration of 1 μg/ml at room temperature (RT) for 10 min. The pictures were taken under a 40× objective lens using the Olympus microscope IX71.

Optimization of LNP with cells

FITC-tagged C18-PEG, DSPE-PEG, and Cholesterol-PEG powder were purchased from Nanocs without further purification. The FITC-tagged PEGylated lipids were dissolved in pure anhydrous ethanol at a final concentration of 1 mM, and stored at –80 °C, respectively. Approximately 10^7 MDA-MB-231 cells were harvested and re-suspended either in 250 μl of Diluent C or 5% human albumin in PBS. 10 nmol of each lipid probe was added into 250 μl of Diluent C before being added to the cell suspension. The samples were mixed gently at 4 °C for 5 min followed by centrifugation at 500*g* for 5 min to remove redundant lipid probes and fixed with 4% paraformaldehyde at 4 °C for 10 min. Then, cells were re-suspended in 1.5 ml of PBS, stained with DAPI solution at concentration of 1 μg/ml at RT for 10 min, thoroughly rinsed with PBS thrice, and finally re-suspended in 500 μl of PBS. 20 μl of cell suspension were added onto glass cover slips for fluorescent imaging. The pictures were taken under a 40× objective lens using the Olympus microscope IX71. The fluorescence intensities were analysed with ImageJ software.

Preparation and characterization of magnetic sub-microparticles

The magnetic Fe3O4@SiO2 core-shell sub-microparticles were synthesized via a modified Stöber sol-gel process[44–48]. Briefly, 30 mg as-prepared MMPs were ultrasonically dispersed in a solution containing 160 ml of ethanol, 40 ml of water and 10 ml of concentrated ammonia (28 wt%). 0.3 ml of tetraethyl orthosilicate (TEOS) was then added dropwise under sonication, followed stirring for 3 h at room temperature. The resulting particles were separated using a magnet, washed with DI water and ethanol thoroughly, and dried at 60 °C for 12 h. To functionalize MMPs with amino groups, 250 mg of MMPs and 250 μl of 3-aminopropyltriethoxysilane (APTES) were ultrasonically dispersed in 30 ml of toluene. The mixture was refluxed for 12 h under a nitrogen atmosphere. Finally, the products were collected, rinsed with toluene and ethanol thrice, and dried at 80 °C overnight. The morphology of MMPs was confirmed under scanning electron microscopy (Zeiss, Sigma). Fourier transform infrared (FTIR) spectra were obtained using a Bruker Vertex V70 over a KBr and then scanned from 400 to 4,000 cm^{-1} at a resolution of 6 cm^{-1}.

5 mg of amine-functionalized MMPs were added in a dimethylformanide (DMF) solution containing 10% pyridine and 1 mM phenyldiisothiocyanate (PDITC) for 2 h. MMPs were then thoroughly washed with DMF, ethanol and DI water thrice. The zeta potential of the MMPs before and after chemical modification was measured using a Zetasizer (Malvern). Approximately 625 μg of NeutrAvidin proteins (Life technologies) in DI water were conjugated to isothiocyanate-grafted MMPs at 37 °C for 1 h followed by blocking with 1% BSA in PBS and washing with PBS thrice. The fresh NeutrAvidin coated MMPs were used for nEVs isolation immediately[49,50].

Isolation of nEVs by using LNP

LP (biotin-tagged DSPE-PEG) powder was dissolved in pure anhydrous ethanol at a final concentration of 1 mM, and stored at –20 °C. The nEVs were labelled with the LP according to the PKH26 labelling protocol, with minor modifications. 100 μl of model samples of nEVs was added into 1 ml of Diluent C. 0.001, 0.01, 0.1, 1, 5, and 10 nmol LP was added to the other 1 ml of Diluent C before being added to the nEVs and the control. The samples were mixed gently at 4 °C for 5 min and then incubated with CP (NeutrAvidin coated MMPs) at RT for 30 min. After isolation, MMPs were rinsed thoroughly with PBS thrice to remove non-specific molecules absorbed on the MMPs surface. The influence of mixing time ranging from 2 to 8 min and the following incubation time ranging from 5 to 30 min were further optimized. The morphology of nEVs -bound MMPs was characterized using SEM.

A triplicate assay of 1, 10, 50, 100, and 200 nmol LP in 500 μl Diluent C were added into 100 μl plasma collected from a healthy volunteer, mixed for 5 min at 4 °C and incubated with MMPs at RT for 10 min. Additionally, 100 μl plasma was added into 30 ml PBS and ultracentrifuged once at 100,000*g* at 4 °C for 2 h. RNA was extracted as before to evaluate the isolation efficiency.

Release of captured nEVs by using biotin

DSPE-PEG-desthiobiotin (Nanocs) in pure anhydrous ethanol was prepared as usual. Following the above-mentioned protocol, nEVs were labelled with DSPE-PEG-Desthiobiotin and captured onto NA-coated MMPs. Surplus uncaptured nEVs were removed by rinsing MMPs with PBS thrice. 20 nmol biotin in PBS was introduced to displace the DSPE-PEG-desthiobiotin. After incubation for 30 min at RT, MMPs were washed with PBS thoroughly by simply using a pipette[51, 52]. The supernatant was collected for RNA extraction. Release efficiency was calculated from the RNA amounts extracted from the supernatant containing released nEVs divided by the total amount of RNA from captured nEVs.

Characterization of nEVs

5 μl of nEVs sample was placed on 400 mesh Formvar-coated copper grids and incubated for 3 min at RT. Excess samples were blotted with filter paper and then negatively stained with filtered aqueous 1% uranyl acetate for 1 min. Stain was blotted dry from the grids with filter paper, and samples were allowed to dry. Samples were then examined in a FEI Tecnai transmission electron microscope (TEM) at an accelerating voltage of 100 kV.

5 μl of nEVs samples were seeded onto poly-l-lysine coated silicon wafer and fixed in 4% paraformaldehyde for 3 h. Subsequently, samples were immersed into 20%, 30%, 50%, 70%, 85%, 95%, and 100% ethanol concentration gradient solution for 15 min (ref. [53]). Samples were lyophilized overnight followed by sputter-coating with gold at RT. The morphology of nEVs was confirmed under Zeiss FESEM.

For cryo-EM, 5 μl of nEVs samples were applied to a 200 Mesh grids (Quantifoil, Ted Pella), blotted for 1 sec with FEI Vitrobot before plunging into liquid ethane, and transferred to a cryo-sample holder. Samples were visualized in FEI Tecnai F20 TEM and FEI Helios NanoLab 660 SEM.

The number of nEVs was measured using Nanosight LM10 (Malvern). nEVs were diluted 1/100, placed in the chamber, and analysed using Nanoparticle Tracking Analysis (NTA) software to count the number of nEVs.

Wound-healing assay

Approximately 3×10^5 MCF-7 cells were seeded into each well of a 24-well plate and were allowed to attach onto the substrate overnight. When confluence reached 100%, a pipette tip was used to scratch the cell monolayer. Detached cells were removed by replacing the medium. Cells were then incubated at 37 °C in 5% CO_2. To educate cells with nEVs, ~8×10^8 released MDA-MB-231 nEVs were added. The width of the wound was monitored under the microscope at 0, 24 and 48 h time points. ImageJ was used to calculate the wound area.

Rough estimation of RNA quantity in nEVs using SYTO RNASelect stain

0, 5, 15, 25, 35, and 45 μl of standardization samples of nEVs were mixed with 5 μl of SYTO RNASelect stain (Life Technologies, US) at concentration of 500 nM. The final volume of the solution was brought to 50 μl with PBS followed by incubation at 37 °C for 20 min. The excitation and emission wavelengths for green fluorescence measurement were at 490 and 530 nm, respectively using a plate reader. In the other group, RNA was extracted from equal amount of nEVs samples. A standard curve of fluorescence from RNA quantity was then constructed. 5 μl of pre-warmed labelling solution was applied to 50 μl samples and incubated for 20 min at 37 °C. When labelling was complete, fluorescence intensity of each sample was directly measured with a plate reader without rinse.

nEV membrane-protein detection using an ELISA-like assay

Approximately 10^{11} nEVs from SK-N-BE(2), MDA-MB-231 and SW620 cells, respectively, were re-suspended in 100 μl of SFM and labelled with 5 nmol of LP following the above protocol. nEVs were directly anchored onto NA coated glass substrate after incubation at RT for 30 min. All samples were fixed with 1× stabilizing fixative (BD, Biosciences) for 10 min followed by PBS rinsing thrice. Surface was blocked with 1% BSA in PBS for 30 min at RT and incubated overnight at 4 °C with the following fluorescence conjugated antibodies against CD9 (Santa Cruz Biotechnology, sc-13118 FITC) and CD326 (EpCAM, Miltenyl Biotec, 130-098-115). Afterwards, samples were thoroughly washed with PBS and observed

under fluorescence microscopy (Olympus). Fluorescence intensity was quantified with ImageJ.

Nucleic acid and protein extraction

RNA preparation was conducted using Trizol (Life technologies, US) according to the manufacturer's instructions. 750 μl of Trizol and 200 μl of Chloroform were added and vigorously mixed with nEVs. After centrifugation, the aqueous phase of the sample was homogenized with 500 μl pure isopropanol and pelletized followed by RNA wash using 1 ml of 75% ethanol. Finally, the RNA pellet was dissolved in 50 μl of RNase free water. The RNA concentration of nEVs was measured using Qubit Fluorometer (Life Technologies, US) or Agilent 2100 Bioanalyzer (Agilent, US).

The DNA was extracted using the QIAamp DNA micro kit (Qiagen, Germany) according to the manufacturer's instructions. Briefly, to conduct DNA extraction from nEVs, 10 μl of proteinase K and 100 μl of lysis buffer were added. After heat inactivation at 56 °C for 10 min, 100 μl of pure ethanol were supplemented. The whole volume was centrifuged in a spin column. After 2 washing steps, the DNA was eluted in 50 μl of AE buffer and stored at −20 °C until PCR amplification.

Protein amount re-suspended in modified RIPA buffer were determined using Micro BCA Protein Assay Kit (Pierce). Isolated nEVs were mixed well with working reagent and incubated at 60 °C for 30 min. The fluorescence intensity of each samples was measured using Infinite M200 Pro plate reader. The protein concentration for each nEVs samples were determined using a BSA standard curve.

To monitor nEV expression of GAPDH and CD63, isolated nEVs were harvested in 8 M urea/2.5% SDS, 5 μg/ml leupeptin, 1 μg/ml pepstatin, and 1 mM phenylmethylsulfonyl fluoride buffer. Samples were loaded according to BCA quantification an analyzed using acrylamide gels. Wet electrophoretic transfer was used to transfer the proteins in the gel onto PVDF membranes (Immobilon P). The protein blot was blocked for 1 h at RT with 5% non-fat dry milk in PBS/0.05% Tween and incubated overnight at 4 °C with the following primary antibodies against GAPDH (Abcam, ab9485) and CD63 (Santa Cruz Biotechnology, sc-15363). Afterwards, secondary antibodies were incubated for 1 h at RT. Samples were washed with PBS/0.05% Tween 20 for 10 min thrice. Blots were developed with chemiluminescent from Pierce[10].

PCR and sequencing

KRAS analysis (466 bp) was performed using the following primers: forward 5′-AAG GCC TGC TGA AAA TGA CTG-3′ and reverse 5′-TCA CAA TAC CAA GAA ACC CAT-3′[10]. EGFR Exon 19 and 21 were performed using the following primers: Exon 19 (372 bp), forward 5′- GCA ATA TCA GCC TTA GGT GCG GCT C-3′, reverse 5′- CAT AGA AAG TGA ACA TTT AGG ATG T G-3′; Exon 21 (300 bp), forward 5′-TGC AGA GCT TCT TCC CAT GA-3′, reverse 5′-GCA TGT GTT AAA CAA TAC AGC-3′[54]. PCR was performed in a 25-μl reaction tube consisting of 12.5 μl GoTaq Green Master Mix (Promega), 10.5 μl of template DNA, 1 μl of each primer. Amplification was carried out under the following conditions: 94 °C for 1 min, 2 cycles of 94 °C for 10 s, 67 °C for 10 s,

70 °C for 10 s; 2 cycles of 94 °C for 10 s, 64 °C for 10 s, 70 °C for 10 s; 2 cycles of 94 °C for 10 s, 61 °C for 10 s, 70 °C for 10s; 55 cycles of 94 °C for 10 s, 60 °C for 10 s, 70 °C for 10 s, endless 4 °C. PCR products were cleaned using the QIAquick PCR Purification Kit (Qiagen) following the manufacturer's instructions and sequenced by Sanger DNA sequencing (Applied Biosystems 3730XL) at Genomics Core Facility service at Penn State University.

Alternatively, PointMan KRAS (codon 12/13) DNA enrichment kit (EKF molecular diagnostics), a real-time PCR kit, was used to enrich mutations. Relevant samples were purified for Sanger sequencing once variant traces were observed in real-time PCR. For EGFR mutant-enriched PCR assay, the 2 μl of the first traditional PCR products of EGFR exon 19 and exon 21 were further digested with Mse I and Msc I at 37 °C for 4 h, respectively. An aliquot was used as a template for the second round of nest PCR amplification under the same conditions as the first round PCR but for 42 cycles. Exon 19 nest PCR (175 bp) primers were: forward 5′-TAA AAT TCC CGT CGC TAT CAA-3′ and reverse 5′-ATG TGG AGA TGA GCA GGG-3′. Exon 21 nest PCR (213 bp) primers were: forward 5′-CAG CAG GGT CTT CTC TGT TTC-3′ and reverse 5′- GAA AAT GCT GGC TGA CCT AAA G-3′. Products were purified and analysed by sequencing.

Whole genome sequencing by NGS

The isolated nEV DNA was mechanically fragmented to 400 bp by using a focused ultrasonicator (Covaris). DNA sequencing was performed at the Biopolymers Facility at Harvard Medical School. The WaferGen DNA prepX kit was used to prepare the sequencing library. Next Generation Sequencing was performed on the Illumina NextSeq 500 platform, paired-end 2×77 bp, to a coverage depth of 3.3×. The data quality was assessed using FastQC. Data was mapped to human genome (hg38) using bwa-mem and coverage files were produced using bedtools. Mapping was visualized suing IGV, and read counts in 10 kbp was calculated with bedtools. Read coverage in 10 kbp bin was plotted in circus plots for each sample. To determine copy number variation (CNV) of the nEVs samples, each NGS data set was downsampled to 10 Mbp. Separately, genomic DNA of the same cell line was prepared without amplification and sequenced by NextSeq to a coverage depth of 0.16×. The CNV plots were generated using open-source web platform Gingko (http://qb.cshl.edu/ginkgo/).

RNA sequencing by NGS

The rRNA-depleted total nEVs RNA were extracted by using the miRNeasy Mini Kit (Qiagen). RNA sequencing was performed at the Genomics Technology Center at NYU medical center. Illumina TruSeq Strandard mRNA kit was used to prepare the mRNA and sRNA sequencing libraries. Sequencing libraries were pooled together and sequenced on the Illumina HiSeq platform, single-end 50 bp. We obtained more than 20 million 51 bp reads for each of the 16 samples (small RNA-seq, $n = 8$; total RNA-seq, $n = 8$). The adapters for small RNA-seq were removed using cutadapt. All the reads were mapped to the human reference genome (GRCh37/hg19) using the STAR aligner (v.2.3.0e r291)[55].The alignment was guided by a Gene Transfer File (GTF version GRCh37.70). The read per million (RPM) normalized BigWig files were generated using Bedtools (v.2.17.0)[56] and the

bedGraphToBigWig tool (v.4). Read count tables were generated using HTSeq (v.0.6.0) based on the Ensembl gene annotation file (Ensembl GTF version GRCh37.70)[57]. All read count tables were then corrected for their library-size differences based on their geometric library-size factors calculated using the DESeq2 R package (v.3.0)[58], and differential expression (DE) analysis was performed. To compare the level of similarity among the samples in our dataset on the basis of their normalized gene expression, we used Euclidean distance-based sample clustering. All downstream statistical analyses and data visualizations were performed in R (v.3.1.1) (http://www.r-project.org/). For PCA and Euclidean distance analyses, we transformed the normalized count data using DESeq2's rlogTransformation function for fixing for infinite log2 (expression values) in genes with zero (or not detected) expression. We employed DESeq's plotPCA function to calculate the first two principle components, and we created the two-dimensional plot using the ggplot2 package. For distance analysis, we used the R dist function to calculate the sample distances in the transformed normalized count data (as explained earlier) by setting the method as Euclidean (default), clustering the samples on the basis of their distance, and visualizing them in heat maps.

LC-MS/MS

Protein concentrations were measured by BCA-protein assay. Approximately 30 μg of proteins were separated by SDS-PAGE using 10% Bis-Tris Nupage gels. Serial gel slices were excised and diced into smaller fragments. Samples were reduced with 10 mM dithiothreitol in 25 mM NH4HCO3 at 56 °C for 1 h and alkylated with 55 mM iodoacetamide for 45 min at RT. In-gel trypsin digestion was performed using 10 ng/μl of sequencing grade modified porcine trypsin (Promega) diluted in 505 mM NH4HCO3 at 37 °C overnight. Peptides were extracted with 0.5% formic acid and 50% acetonitrile. Following evaporation of acetonitrile, peptides were purified using a ZipTipC18 column (Millipore). The volume of each eluted sample was reduced in a Speedvac to 5 μl to evaporate acetonitrile and adjusted to 20 μl with 0.1% formic acid prior to LC–MS/MS analysis. An AB SCIEX TripleTOF 5600 System (Foster City) equipped with an Eksigent nanoLC Ultra and ChiPLC-nanoflex (Eksigent) in Trap Elute configuration was employed for LC-MS measurement. The acquired mass spectrometric raw data was processed using ProteinPilot 5.0 software (AB SCIEX) with the Paragon search mode. The ProteinPilot Descriptive Statistics Template (PDST, AB SCIEX) was used for alignment of multiple results and evaluation of the false discovery rate.

Data availability

The authors declare that all data supporting the findings of this study are available within the paper and its supplementary information. Source data for the figures in this study are available in figshare with the identifier 10.6084/m9.figshare.4728856 (ref. [59]).

Supplementary Material

Refer to Web version on PubMed Central for supplementary material.

Acknowledgments

S.-Y.Z. thanks the Penn State Materials Research Institute, the Huck Institute of Life Sciences, the Penn State Hershey Cancer Institute, the Penn State proteomic and mass spectrometry facilities at Hershey and University Park, the Penn State Microscopy and Cytometry facility, and the Penn State Genomics Facility for their support. This work was partially supported by the Pennsylvania State University start-up fund and the National Cancer Institute of the National Institutes of Health under Award Number DP2CA174508. We would like to thank the Applied Bioinformatics Center (BFX) at the NYU School of Medicine for providing bioinformatics support and for helping with the analysis and interpretation of the data. This work has used computing resources at the High Performance Computing Facility (HPCF) of the Center for Health Informatics and Bioinformatics at the NYU Langone Medical Center. We also thank the Genome Technology Center (GTC) for expert library preparation and sequencing. This shared resource is partially supported by the Cancer Center Support Grant, P30CA016087, at the Laura and Isaac Perlmutter Cancer Center. We would like to thank Dr. Susan Hafenstein at Penn State Hershey for helpful discussions on cryo-EM and Dr. Chengzhong Zhang at the Dana-Farber Cancer Institute for his advice on genomic analysis.

References

1. Colombo M, Raposo G, Thery C. Biogenesis, secretion, and intercellular interactions of exosomes and other extracellular vesicles. Annu Rev Cell Dev Biol. 2014; 30:255–289. [PubMed: 25288114]
2. Raposo G, Stoorvogel W. Extracellular vesicles: exosomes, microvesicles, and friends. J Cell Biol. 2013; 200:373–383. [PubMed: 23420871]
3. Cocucci E, Meldolesi J. Ectosomes and exosomes: shedding the confusion between extracellular vesicles. Trends Cell Biol. 25:364–372.
4. Yáñez-Mó M, et al. Biological properties of extracellular vesicles and their physiological functions. J Extracell Vesicles. 2015; 4:27066. [PubMed: 25979354]
5. Thery C, Zitvogel L, Amigorena S. Exosomes: composition, biogenesis and function. Nat Rev Immunol. 2002; 2:569–579. [PubMed: 12154376]
6. Li Y, Shen Z, Yu XY. Transport of microRNAs via exosomes. Nat Rev Cardiol. 2015; 12:198–198.
7. Alderton GK. Diagnosis: Fishing for exosomes. Nat Rev Cancer. 2015; 15:453–453. [PubMed: 26205334]
8. Melo SA, et al. Glypican-1 identifies cancer exosomes and detects early pancreatic cancer. Nature. 2015; 523:177–182. [PubMed: 26106858]
9. Thakur BK, et al. Double-stranded DNA in exosomes: a novel biomarker in cancer detection. Cell Res. 2014; 24:766–769. [PubMed: 24710597]
10. Kahlert C, et al. Identification of Double-stranded Genomic DNA Spanning All Chromosomes with Mutated KRAS and p53 DNA in the Serum Exosomes of Patients with Pancreatic Cancer. J Biol Chem. 2014; 289:3869–3875. [PubMed: 24398677]
11. Costa-Silva B, et al. Pancreatic cancer exosomes initiate pre-metastatic niche formation in the liver. Nat Cell Biol. 2015; 17:816–826. [PubMed: 25985394]
12. Melo SA, et al. Cancer Exosomes Perform Cell-Independent MicroRNA Biogenesis and Promote Tumorigenesis. Cancer Cell. 2014; 26:707–721. [PubMed: 25446899]
13. Yeo RWY, et al. Mesenchymal stem cell: An efficient mass producer of exosomes for drug delivery. Adv Drug Deliv Rev. 2013; 65:336–341. [PubMed: 22780955]
14. Lai RC, Yeo RWY, Tan KH, Lim SK. Exosomes for drug delivery — a novel application for the mesenchymal stem cell. Biotechnol Adv. 2013; 31:543–551. [PubMed: 22959595]
15. Azmi AS, Bao B, Sarkar FH. Exosomes in cancer development, metastasis, and drug resistance: a comprehensive review. Cancer Metastasis Rev. 2013; 32:623–642. [PubMed: 23709120]
16. Ohno, S-i, et al. Systemically Injected Exosomes Targeted to EGFR Deliver Antitumor MicroRNA to Breast Cancer Cells. Mol Ther. 2013; 21:185–191. [PubMed: 23032975]
17. Liga A, Vliegenthart ADB, Oosthuyzen W, Dear JW, Kersaudy-Kerhoas M. Exosome isolation: a microfluidic road-map. Lab Chip. 2015; 15:2388–2394. [PubMed: 25940789]
18. Christianson HC, Svensson KJ, van Kuppevelt TH, Li JP, Belting M. Cancer cell exosomes depend on cell-surface heparan sulfate proteoglycans for their internalization and functional activity. Proc Natl Acad Sci USA. 2013; 110:17380–17385. [PubMed: 24101524]

19. Bechstein DJB, et al. High performance wash-free magnetic bioassays through microfluidically enhanced particle specificity. Sci Rep. 2015; 5:11693. [PubMed: 26123868]
20. Caballero JN, Frenette G, Belleannée C, Sullivan R. CD9-Positive Microvesicles Mediate the Transfer of Molecules to Bovine Spermatozoa during Epididymal Maturation. PLoS ONE. 2013; 8:e65364. [PubMed: 23785420]
21. Tauro BJ, et al. Two Distinct Populations of Exosomes Are Released from LIM1863 Colon Carcinoma Cell-derived Organoids. Mol Cell Proteomics. 2013; 12:587–598. [PubMed: 23230278]
22. Thery C, et al. Indirect activation of naive CD4+ T cells by dendritic cell-derived exosomes. Nat Immunol. 2002; 3:1156–1162. [PubMed: 12426563]
23. Lambertz U, et al. Small RNAs derived from tRNAs and rRNAs are highly enriched in exosomes from both old and new world Leishmania providing evidence for conserved exosomal RNA Packaging. BMC Genomics. 2015; 16:1–26. [PubMed: 25553907]
24. Gormally E, Caboux E, Vineis P, Hainaut P. Circulating free DNA in plasma or serum as biomarker of carcinogenesis: practical aspects and biological significance. Mutat Res. 2007; 635:105–117. [PubMed: 17257890]
25. Wei Z, Batagov AO, Carter DR, Krichevsky AM. Fetal bovine serum RNA interferes with the cell culture derived extracellular RNA. Sci Rep. 2016; 6:31175. [PubMed: 27503761]
26. Kowal J, et al. Proteomic comparison defines novel markers to characterize heterogeneous populations of extracellular vesicle subtypes. Proc Natl Acad Sci USA. 2016; 113:E968–E977. [PubMed: 26858453]
27. Asano H, et al. Detection of EGFR Gene Mutation in Lung Cancer by Mutant-Enriched Polymerase Chain Reaction Assay. Clin Cancer Res. 2006; 12:43–48. [PubMed: 16397022]
28. Vlassov AV, Magdaleno S, Setterquist R, Conrad R. Exosomes: Current knowledge of their composition, biological functions, and diagnostic and therapeutic potentials. Biochim Biophys Acta. 2012; 1820:940–948. [PubMed: 22503788]
29. Klymchenko, Andrey S., Kreder, R. Fluorescent Probes for Lipid Rafts: From Model Membranes to Living Cells. Chem Biol. 2014; 21:97–113. [PubMed: 24361047]
30. Wijesinghe D, Arachchige MCM, Lu A, Reshetnyak YK, Andreev OA. pH dependent transfer of nano-pores into membrane of cancer cells to induce apoptosis. Sci Rep. 2013; 3:3560. [PubMed: 24356337]
31. Lobb RJ, et al. Optimized exosome isolation protocol for cell culture supernatant and human plasma. J Extracell Vesicles. 2015; 4:27031. [PubMed: 26194179]
32. Jeong S, et al. Integrated Magneto–Electrochemical Sensor for Exosome Analysis. ACS Nano. 2016; 10:1802–1809. [PubMed: 26808216]
33. Im H, et al. Label-free detection and molecular profiling of exosomes with a nano-plasmonic sensor. Nat Biotechnol. 2014; 32:490–495. [PubMed: 24752081]
34. Zhao Z, Yang Y, Zeng Y, He M. A microfluidic ExoSearch chip for multiplexed exosome detection towards blood-based ovarian cancer diagnosis. Lab Chip. 2016; 16:489–496. [PubMed: 26645590]
35. Weber RJ, Liang SI, Selden NS, Desai TA, Gartner ZJ. Efficient Targeting of Fatty-Acid Modified Oligonucleotides to Live Cell Membranes through Stepwise Assembly. Biomacromolecules. 2014; 15:4621–4626. [PubMed: 25325667]
36. Charbonneau DM, Tajmir-Riahi HA. Study on the Interaction of Cationic Lipids with Bovine Serum Albumin. J Phys Chem B. 2010; 114:1148–1155. [PubMed: 19961210]
37. Bobrie A, Colombo M, Krumeich S, Raposo G, Théry C. Diverse subpopulations of vesicles secreted by different intracellular mechanisms are present in exosome preparations obtained by differential ultracentrifugation. J Extracell Vesicles. 2012; 1:18397.
38. Van Niel G, et al. Intestinal epithelial cells secrete exosome–like vesicles. Gastroenterology. 2001; 121:337–349. [PubMed: 11487543]
39. Colombo M, et al. Analysis of ESCRT functions in exosome biogenesis, composition and secretion highlights the heterogeneity of extracellular vesicles. J Cell Sci. 2013; 126:5553–5565. [PubMed: 24105262]
40. Rupp AK, et al. Loss of EpCAM expression in breast cancer derived serum exosomes: role of proteolytic cleavage. Gynecol Oncol. 2011; 122:437–446. [PubMed: 21601258]

41. Boch C, et al. The frequency of EGFR and KRAS mutations in non-small cell lung cancer (NSCLC): routine screening data for central Europe from a cohort study. BMJ Open. 2013; 3:e002560.
42. Bettegowda C, et al. Detection of Circulating Tumor DNA in Early- and Late-Stage Human Malignancies. Sci Transl Med. 2014; 6:224ra224.
43. Newman AM, et al. An ultrasensitive method for quantitating circulating tumor DNA with broad patient coverage. Nat Med. 2014; 20:548–554. [PubMed: 24705333]
44. Cheng G, et al. The GO/rGO-Fe3O4 composites with good water-dispersibility and fast magnetic response for effective immobilization and enrichment of biomolecules. J Mater Chem. 2012; 22:21998–22004.
45. Cheng G, Zhang JL, Liu YL, Sun DH, Ni JZ. Synthesis of novel Fe3O4@SiO2@CeO2 microspheres with mesoporous shell for phosphopeptide capturing and labeling. Chem Comm. 2011; 47:5732–5734. [PubMed: 21503338]
46. Deng Y, Qi D, Deng C, Zhang X, Zhao D. Superparamagnetic high-magnetization microspheres with an Fe3O4@ SiO2 core and perpendicularly aligned mesoporous SiO2 shell for removal of microcystins. J Am Chem Soc. 2008; 130:28–29. [PubMed: 18076180]
47. Morel AL, et al. Sonochemical approach to the synthesis of Fe3O4@ SiO2 core− shell nanoparticles with tunable properties. Acs Nano. 2008; 2:847–856. [PubMed: 19206481]
48. Ding H, et al. Fe3O4@ SiO2 core/shell nanoparticles: the silica coating regulations with a single core for different core sizes and shell thicknesses. Chem Mater. 2012; 24:4572–4580.
49. Wan Y, et al. Surface-Immobilized Aptamers for Cancer Cell Isolation and Microscopic Cytology. Cancer Res. 2010; 70:9371–9380. [PubMed: 21062984]
50. Wang S, Wan Y, Liu Y. Effects of nanopillar array diameter and spacing on cancer cell capture and cell behaviors. Nanoscale. 2014; 6:12482–12489. [PubMed: 25137436]
51. Xue P, et al. Isolation and elution of Hep3B circulating tumor cells using a dual-functional herringbone chip. Microfluid Nanofluidics. 2014; 16:605–612.
52. Lu NN, et al. Biotin-Triggered Decomposable Immunomagnetic Beads for Capture and Release of Circulating Tumor Cells. ACS Appl Mater Interfaces. 2015; 7:8817–8826. [PubMed: 25853336]
53. Wan Y, et al. Nanotextured substrates with immobilized aptamers for cancer cell isolation and cytology. Cancer. 2012; 118:1145–1154. [PubMed: 21766299]
54. Lynch TJ, et al. Activating Mutations in the Epidermal Growth Factor Receptor Underlying Responsiveness of Non–Small-Cell Lung Cancer to Gefitinib. N Engl J Med. 2004; 350:2129–2139. [PubMed: 15118073]
55. Dobin A, et al. STAR: ultrafast universal RNA-seq aligner. Bioinformatics. 2013; 29:15–21. [PubMed: 23104886]
56. Quinlan AR, Hall IM. BEDTools: a flexible suite of utilities for comparing genomic features. Bioinformatics. 2010; 26:841–842. [PubMed: 20110278]
57. Alam S, et al. The eleventh and twelfth data releases of the Sloan Digital Sky Survey: Final data from SDSS-III. Astrophys J Suppl Ser. 2015; 219:12.
58. Anders S, Huber W. Differential expression analysis for sequence count data. Genome Biol. 2010; 11:1.
59. Wan, Y., et al. Dataset for Rapid isolation of extracellular vesicles via lipid nanoprobes. figshare. 2017. http://dx.doi.org/10.6084/m9.figshare.4728856

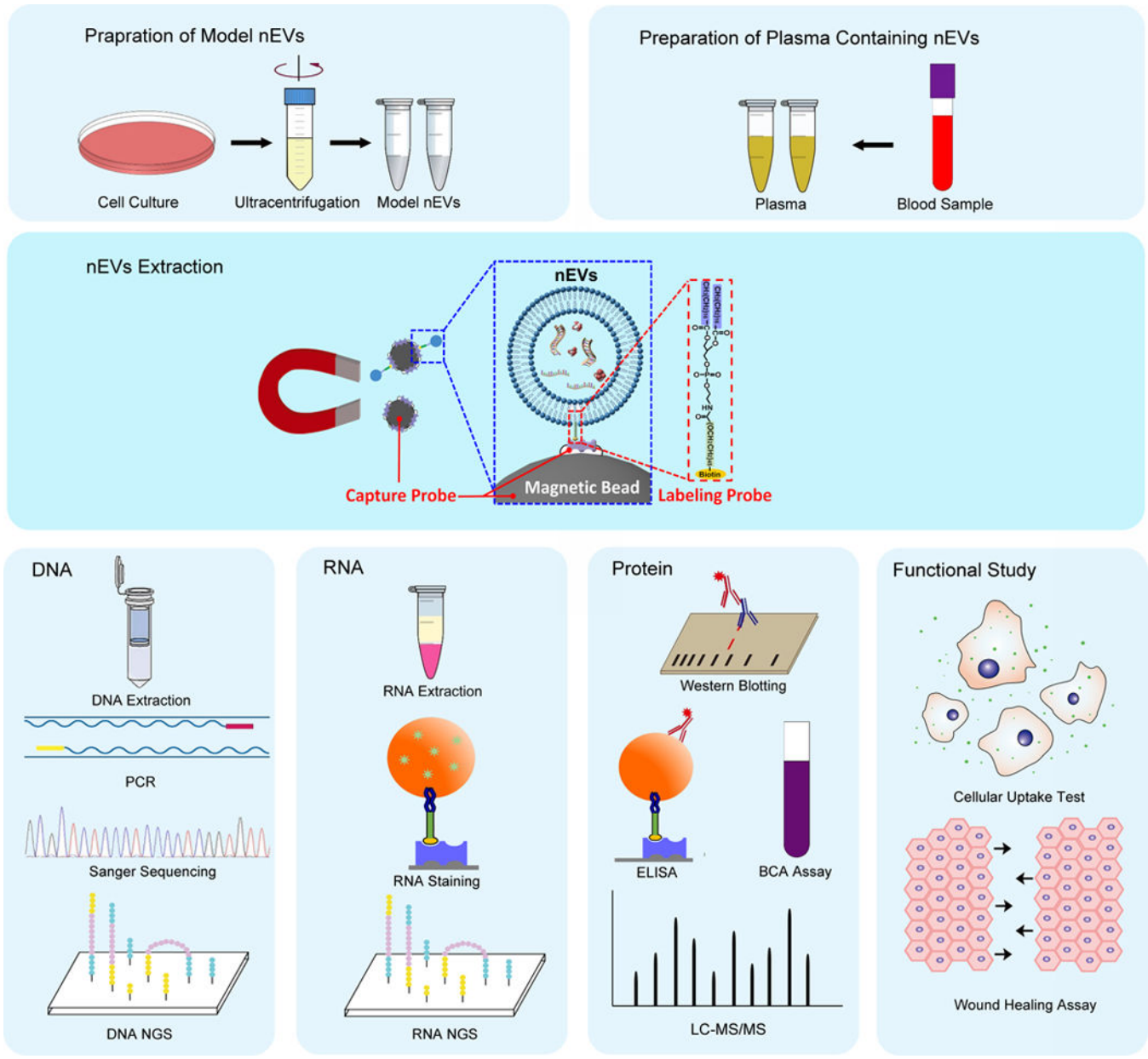

Figure 1. Schematic of the LNP system for nEV enrichment and downstream analyses

Top and Middle, nEVs from either serum-free cell-culture medium or blood plasma are marked with the labelling probe (top), followed by magnetic separation with the capture probe (middle). Bottom, nEVs and their cargo contents can then be analysed by different methods, such as PCR, Sanger sequencing and NGS sequencing for DNA, RNA staining and RNA NGS for RNA, enzyme-linked immunosorbent assay (ELISA), the bicinchoninic acid assay (BCA) and LC-MS/MS for proteins, and cellular-uptake and wound-healing assays for functionality.

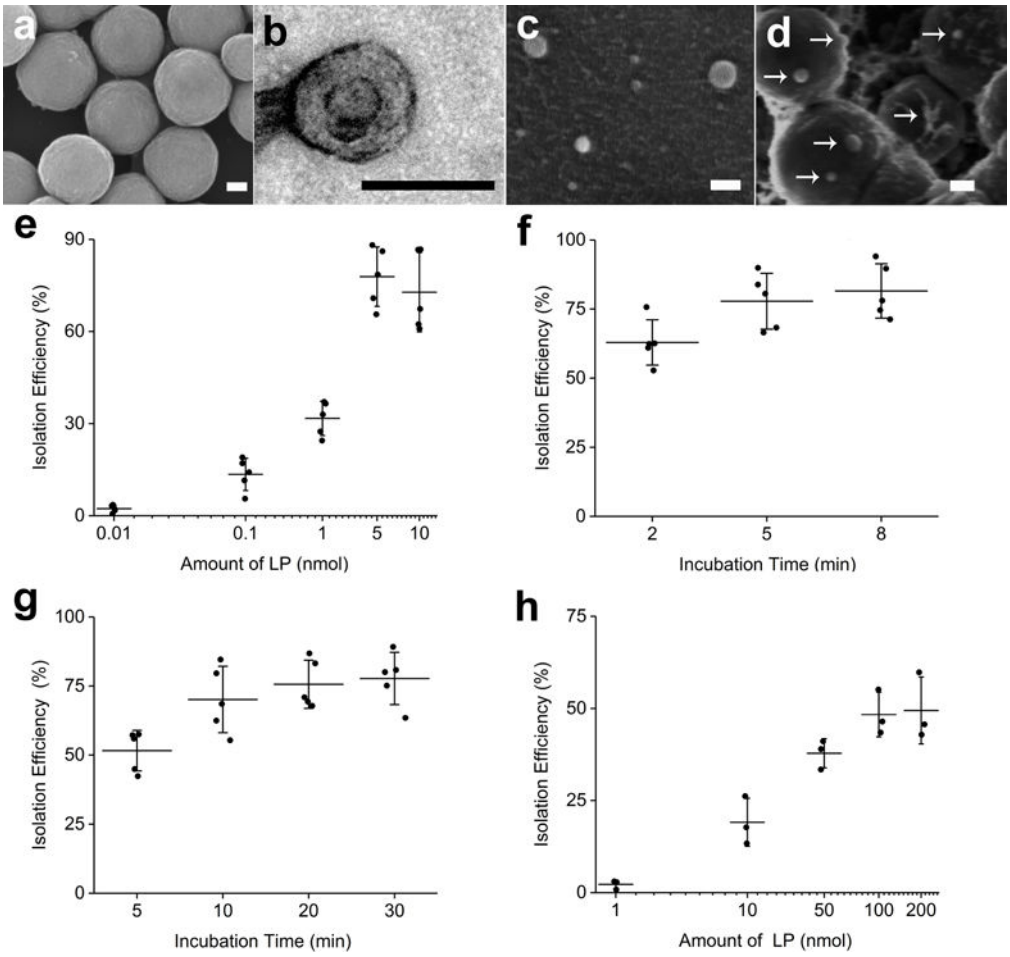

Figure 2. Morphological characterization of the materials and optimization of the LNP system for isolation efficiency

a–d, Morphological characterization by EM. Scale bars, 100 nm. **a**, SEM image of synthesized MMPs. **b,c**, TEM (**b**) and cryo-SEM (**c**) images showing the morphology of nEVs. **d**, Cryo-SEM image showing that LP-labelled MDA-MB-231 nEVs (arrowhead) are captured on the surface of the CPs. **e–g**, Isolation efficiency of MDA-MB-231 nEVs as a function of LP amount (**e**), incubation time of the LPs with model samples (**f**), and incubation time of the LPs and CPs (**g**); Error bars, mean ± s.e.m. (n = 5). **h**, Isolation efficiency of nEVs from healthy-donor plasma samples as a function of LP amount. Error bars, mean ± s.e.m. (n = 3).

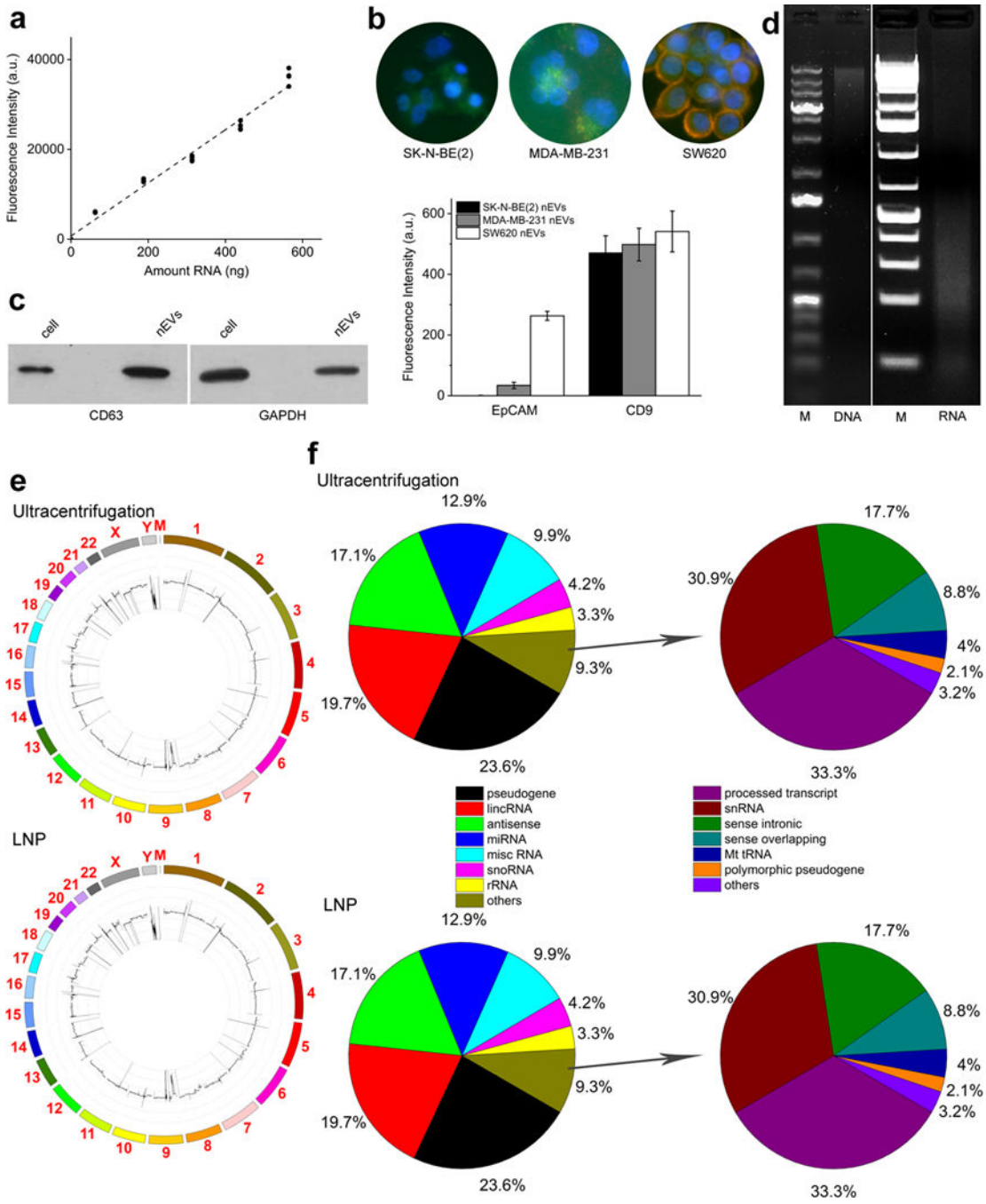

Figure 3. Isolated nEVs provide flexibility in downstream molecular analyses

a, LP-labelled nEVs were enriched on NA-coated well plates followed by RNA-dye staining. Fluorescence intensity increased in direct proportion to total RNA contained in integral nEVs. Error bars, mean ± s.e.m. (n = 4). **b**, Fluorescently labelled CD9 and EpCAM antibodies were used to detect relevant protein expression of model nEVs released from SK-N-BE(2), MDA-MB-231 and SW620 cells. Error bars, mean ± s.e.m. (n = 20). Top insets show CD9 (green), EpCAM (red) and DAPI (blue) staining of the cells. **c**, CD63 and GAPDH proteins were extracted and identified from isolated nEVs by western blot. **d**, DNA

and RNA were extracted from isolated nEVs and identified with 2% agarose gel electrophoresis. 1 kbp DNA ladders (labelled as M) indicate the length of fragments. **e**, Circos plots of nEV DNA of MDA-MB-231 cells isolated by ultracentrifugation (top) and by the LNP (bottom). DNA was sequenced by NGS with 3.3× depth of coverage, mapped to human genome, and plotted with a size window of 100 kbp. Read coverage is expressed in natural logarithmic scale with 0, 3, 6, 9, 12, and 15 reads, from the inside to the outside. **f**, Pie charts depicting different RNA species and their mapped read-count distributions from MDA-MB-231 nEVs isolated by ultracentrifugation (top) and by the LNP (bottom). Left, full-scale plots; Right, plots zooming into low-abundance RNA species (labelled as ‘others’ in the full-scale plots).

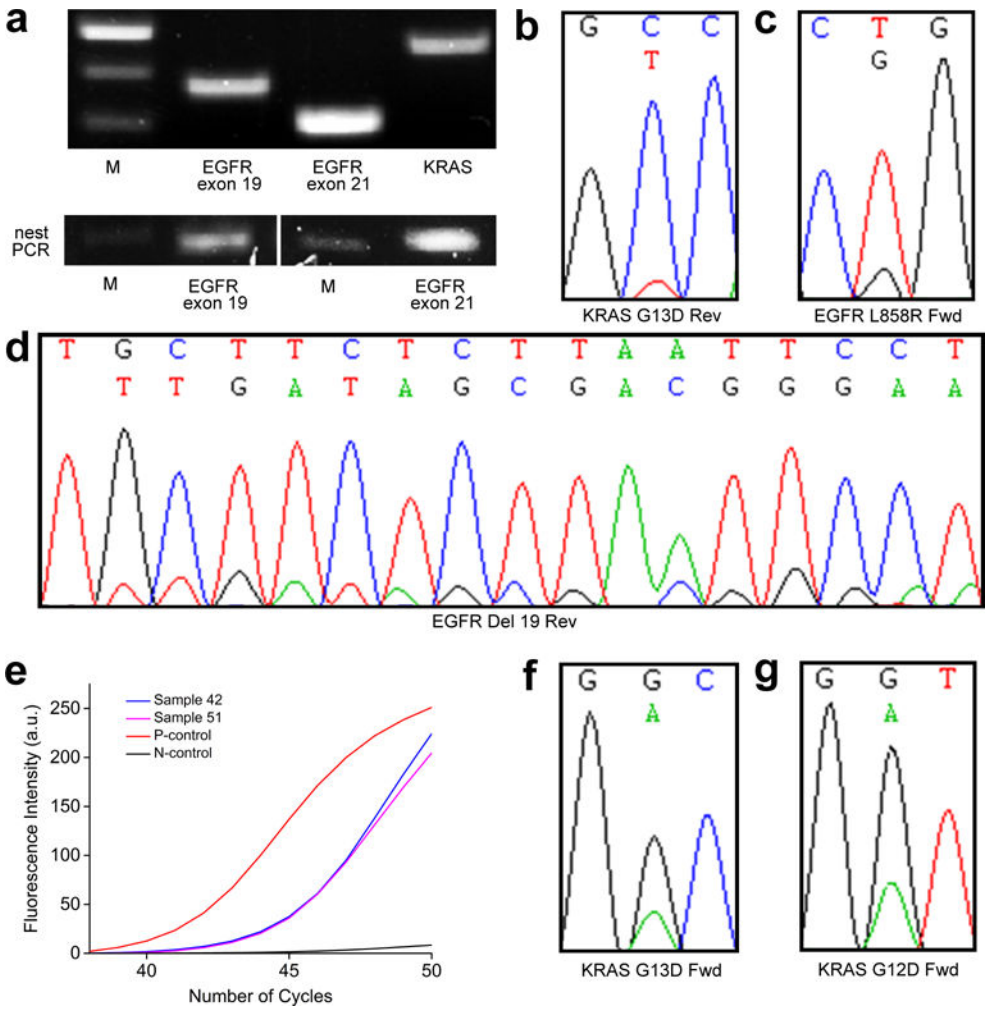

Figure 4. Detection of DNA mutations in nEVs isolated from plasma samples from NSCLC patients

a, Gel electrophoresis of EGFR and KRAS DNA fragments after a first round of PCR amplification (top) and a second round of mutant-enriched nested PCR (bottom). nEVs were isolated from the plasma of patient 24 followed by DNA extraction and PCR amplification. To detect EGFR mutations in exons 19 and 21, first-batch PCR products were enzymatically digested and used as template for the next mutant-enriched nested PCR. M, 1 kbp DNA ladders. **b**, A KRAS G13D point mutation was detected in the plasma sample of patient 42 by using direct sequencing of traditional PCR products with reverse primers. **c**, A EGFR L858R point mutation in exon 21 was identified in the plasma sample of patient 28 by sequencing the nested PCR products. **d**, A deletion mutation in the EGFR exon 19 was identified in the plasma sample of patient 29 by sequencing the nested PCR products. **e**, Real-time PCR profiles of samples from patients 42 and 51, alongside positive and negative controls. Real-time PCR was performed on all nEV DNA samples to enrich for KRAS mutations. **f**, Sequencing of the real-time PCR product confirmed the KRAS G13D mutation in the plasma sample of patient 42. **g**, Sequencing of the real-time PCR product detected a KRAS G12D mutation in the plasma of patient 51.

Nat Biomed Eng. Author manuscript; available in PMC 2017 October 10.

Table 1

Detection of *KRAS* mutations and *EGFR exon 19 and 21* mutations among 19 samples from NSCLC patients.

Patient No.	Age	Sex	Tissue Source	EGFR Mutation		KRAS Mutation	
				nEVs	Tissue	nEVs	Tissue
24	61	M	lung	WT	WT	WT	WT
25	58	M	small bowel	WT	WT	**WT**	**G12C**
26	58	F	lymph node	WT	WT	WT	WT
27	60	F	lung	WT	WT	**WT**	**G12C**
28	90	M	NA	**exon 21 L858R**	**NA**	WT	NA
29	65	F	lymph node	**exon 19 Del**	**exon 19 Del**	WT	WT
30	66	M	bone	WT	WT	WT	WT
31	50	M	lymph node	WT	WT	WT	WT
32	79	F	NA	WT	NA	WT	NA
36	65	F	lung	WT	WT	WT	WT
37	82	F	lung	WT	WT	WT	WT
42	70	F	lymph node	WT	WT	**G13D**	**NA**
50	70	M	lymph node	WT	WT	**WT**	**G12V**
51	70	M	pleura effusion	WT	WT	**G12D**	**G12D**
52	74	M	liver	WT	WT	WT	WT
54	53	M	lung	WT	WT	WT	WT
55	86	F	lung	WT	WT	WT	WT
56	72	F	NA	WT	NA	WT	NA
58	65	M	pleura effusion	WT	WT	WT	WT

Bold text indicates detected mutations.

WT, wild type; Del, deletion; NA, not available.